

ADVANCED MATERIALS

Supporting Information

for *Adv. Mater.*, DOI: 10.1002/adma.201707122

Multidimensional Synergistic Nanoarchitecture Exhibiting
Highly Stable and Ultrafast Sodium-Ion Storage

Shuangshuang Tan, Yalong Jiang, Qiulong Wei, Qianming
Huang, Yuhang Dai, Fangyu Xiong, Qidong Li, Qinyou An, Xu
Xu, Zizhong Zhu, Xuedong Bai,* and Liqiang Mai**

Supporting Information

Multidimensional Synergistic Nanoarchitecture Exhibiting Highly Stable and Ultrafast Sodium Ion Storage

Shuangshuang Tan, Yalong Jiang, Qiulong Wei, Qianming Huang, Yuhang Dai, Fangyu Xiong, Qidong Li, Qinyou An, Xu Xu, Zizhong Zhu, Xuedong Bai*, Liqiang Mai**

Mr. S. Tan, Mr. Y. Jiang, Dr. Q. Wei, Mr. Y. Dai, Mr. F. Xiong, Mr. Q. Li, Prof. Q. An, Dr. X. Xu, Prof. L. Mai

State Key Laboratory of Advanced Technology for Materials Synthesis and Processing, International School of Materials Science and Engineering, Wuhan University of Technology, Wuhan 430070, Hubei, China

Dr. Q. Wei

Department of Materials Science and Engineering, University of California Los Angeles, CA 90095-1595, USA

E-mail: qlwei@ucla.edu E-mail: mlq518@whut.edu.cn

Dr. Q. Huang, Prof. X. Bai

Beijing National Laboratory for Condensed Matter Physics and Institute of Physics, Chinese academy of Sciences, Beijing 100190, China

E-mail: xdbai@iphy.ac.cn

Prof. Z. Zhu

Department of Physics and Institute of Theoretical Physics and Astrophysics, Xiamen University, Xiamen 361005, China

Prof. L. Mai

Department of Chemistry, University of California, Berkeley, California 94720, USA

Materials and Methods

Synthesis of VO_x-NTs. VO_x-NTs were prepared by a simple mixed solvothermal method similar to a previously reported method⁴¹. First, 0.8 mmol of V₂O₅ powder and cetylamine were dispersed in 30 mL of deionized water and alcohol, respectively, and the two solutions were mixed through magnetic stirring for 1 h. The resulting suspension was then transferred to a Teflon-lined autoclave with a stainless steel shell. The autoclave was kept at 180 °C for 36 h, and then allowed to cool to room temperature naturally. The final black product was washed with alcohol and distilled water, and then dried at 70 °C for 24 h.

Synthesis of V₂O₃C-C-NTsCrGO. GO was prepared by a modified Hummer's method. VO_x-NTs (200 mg) were dispersed in 5 mL of alcohol, 5 mL of an aqueous GO dispersion (2 mg/mL) was added, and then mixture was stirred for 10 min. Then, 10 mg of cetyltrimethyl ammonium bromide (CTAB) was added into the mixed solution. After 10 min, the mixed solution was subjected to ultrasonic treatment for 1 h and then centrifuged at 10000 rpm to isolate the black precipitate. Next, the mixture was rapidly cooled in liquid nitrogen and freeze-dried for 48 h. Finally, the product was annealed in Ar/H₂ (95:5) at 500 °C (2 °C min⁻¹) for 8 h to obtain the V₂O₃C-C-NTsCrGO anode material.

Synthesis of V₂O₃C-C-NTs. The synthetic process for the V₂O₃C-C-NTs was the same as that for V₂O₃C-C-NTsCrGO except that GO was not added.

Synthesis of V₂O₃CrGO. First, 160 mg of NH₄VO₃ powders was dissolved in an aqueous GO suspension (8 mL, 2 mg mL⁻¹), and then 2 mL of NH₃·H₂O was added. After 1h of ultrasonication, the mixed solution was transferred to a 25 mL Teflon-lined autoclave. The autoclave was kept at 180 °C for 12 h and then allowed to cool to room temperature naturally. Finally, the obtained hydrogel was freeze-dried and calcinated at 500 °C (5 °C min⁻¹) for 1.5 h in

H₂/Ar (5%/95%). Based on the CHN elemental analysis, the carbon content of V₂O₃⊂rGO was 39.5 wt%.

Synthesis of V₂O₃-NPs. V₂O₃⊂C-NTs were annealed in air to remove the carbon matrixes at 400 °C (2 °C min⁻¹) for 3 h. Then the products were reduced in Ar/H₂ (95:5) at 500 °C (2 °C min⁻¹) for 8 h to obtain V₂O₃-NPs materials. V₂O₃-Bluks is purchased from Alfa Aesar and used as received.

Material characterization. XRD data of the samples were collected with a D8 Advance X-ray diffractometer with an area detector using Cu K α radiation ($\lambda = 1.5418 \text{ \AA}$) in a 2θ range from 5° to 70°. The microstructures were observed by FESEM (JEOL-7100F). TEM, HRTEM, and STEM-HAADF images and STEM-energy dispersive X-ray spectroscopy (EDX) maps were recorded by using a Titan G2 60-300 instrument with an image corrector. Raman spectra were obtained using a Renishaw INVIA micro-Raman spectroscopy system and FT-IR spectra were obtained using a Nexus system. XPS measurements were performed using a VG MultiLab 2000 instrument. BET surface areas were measured using a Tristar II 3020 instrument by the adsorption of nitrogen at 77 K. The tested electrodes were prepared for *ex situ* characterization by taking apart the coin cells in a glove box filled with pure argon gas. For *ex situ* XPS characterization, the electrode materials were washed with dimethyl carbonate (DMC) and alcohol and dried in an argon-filled glove-box for 24h. For *ex situ* SEM and TEM experiments, the electrode materials were washed with DMC and alcohol and then dispersed in alcohol through ultrasonication. To obtain the undisturbed *ex situ* SEM images of the V₂O₃⊂C-NTs, acetylene black particles were not added into the electrode.

***In situ* TEM observation.** A tungsten tip covered with V₂O₃⊂C-NTs or V₂O₃⊂C-NTs⊂rGO was loaded on the TEM-STM holder as an electrode. Sodium metal with a grown Na₂O layer was mounted on a piezo-driven biasing probe to serve as the Na source, and a thin Na₂O layer served

as the solid electrolyte. The samples were brought into contact with the Na₂O/Na particles, and a high voltage bias of -5 V was applied by means of a potentiostat to drive the sodiation reaction. The potential was larger than that used in the tests of Na⁺ ion half-cells due to the necessity to drive the Na⁺ ions through the solid electrolyte and carbon layer.

Electrochemical Measurements. The electrochemical properties were characterized in 2016-type coin cells with Na metal foil as the anode. The anode electrodes were composed of 70% active material, 25% acetylene black and 5% carboxymethyl cellulose (CMC) binder. The slurry was casted onto Cu foil and dried in a vacuum oven at 120 °C for 12 h. The electrode loading was 1–1.5 mg/cm². A solution (1 M) of NaClO₄ in ethylene carbonate/DMC (EC/DMC) (1:1 v/v) + 5% fluoroethylene carbonate (FEC) was used as the electrolyte. The cells were assembled in an argon-filled glove box. Galvanostatic charge/discharge measurements were performed with a multichannel battery testing system (LAND CT2001A), and electrochemical impedance spectroscopy (EIS) were conducted with an Autolab potentiostat galvanostat (PGSTAT302N). Cyclic voltammetry was conducted with a CHI 1000C electrochemical workstation. All measurements were carried out at room temperature.

DFT calculations. The present calculations were carried out by using the projector augmented wave (PAW)^[1] method within DFT, as implemented in the Vienna ab initio simulation package (VASP)^[2,3]. The generalized gradient approximation (GGA) in the form of the Perdew-Burke-Ernzerhof (PBE)^[4] was used to treat the exchange-correlation energy. A kinetic energy cutoff of 500 eV was used for wave functions expanded in the plane wave basis. All atoms were allowed to relax until the forces were less than 0.05 eV Å⁻¹. For the Brillouin-zone sampling, 6×6×6 k-points were adopted to ensure convergence of the total energy. Ultrasoft pseudopotentials were used to describe the interactions of the ionic core and valence electrons. The valence states considered in this study were V 3d³4s², O 2s²2p⁴ and Na 2p⁶3s¹. A unit cell of V₂O₃ crystal with a

periodic structure was used in the DFT calculations. The V_2O_3 crystal had a rhombohedral structure and belonged to the space group R-3c.

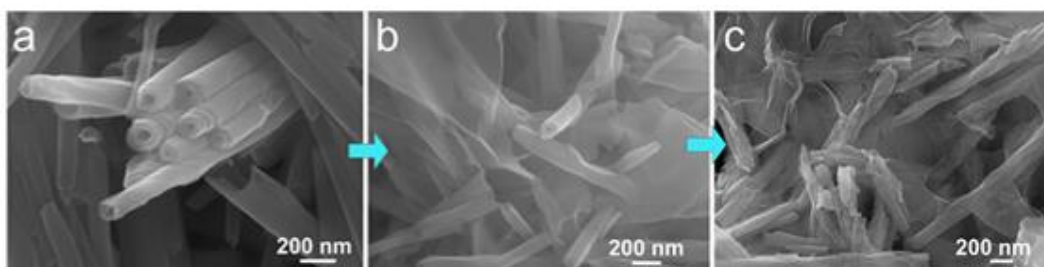


Figure S1. High-resolution SEM images. (a) VO_x -NTs, (b) VO_x -NTs@GO and (c) V_2O_3 @C-NTs@rGO.

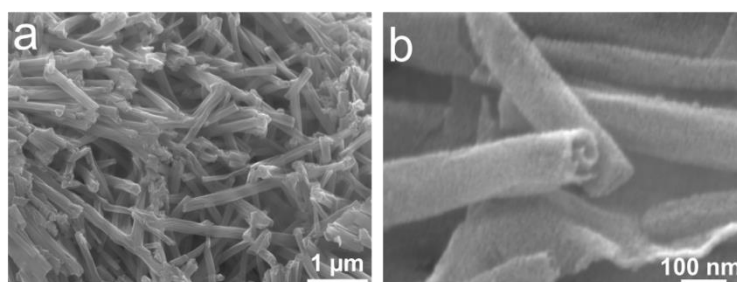


Figure S2. SEM images of the V_2O_3 @C-NTs. An unbroken tube-shaped morphology was obtained after annealing.

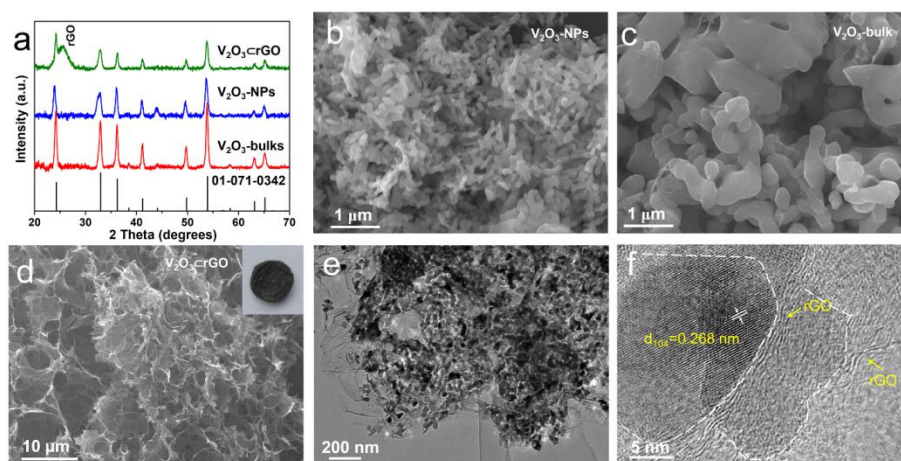


Figure S3. Characterization of V_2O_3 @rGO, V_2O_3 NPs and V_2O_3 bulks. (a) XRD patterns of V_2O_3 @rGO, V_2O_3 NPs and V_2O_3 bulks. SEM images of V_2O_3 NPs (b), V_2O_3 bulks (c) and V_2O_3 @rGO. (d) The inset in (d) is an optical images of V_2O_3 @rGO. (e, f) TEM and HRTEM images of V_2O_3 @rGO.

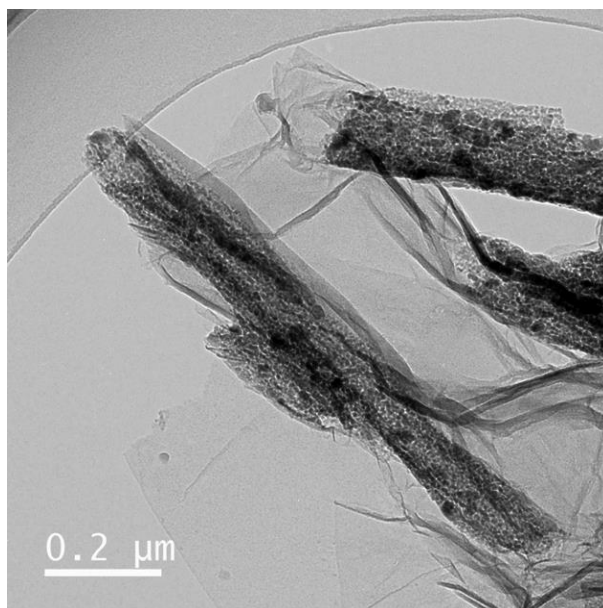


Figure S4. TEM image of $V_2O_3/C-NTs/rGO$ showing the porous nature of the $V_2O_3/C-NTs$.

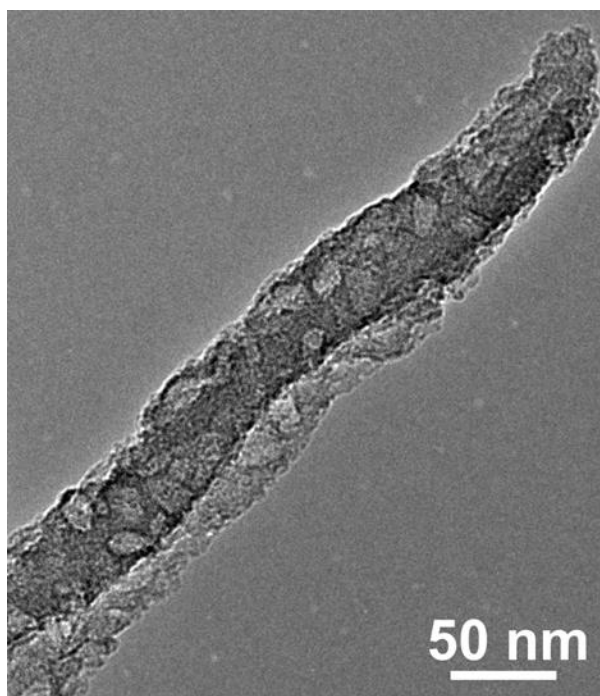


Figure S5. TEM image of the $V_2O_3/C-NTs$ etched by hydrochloric acid showing the porous tube-shaped carbon framework. The concentration of hydrochloric acid was 0.5 mol/L.

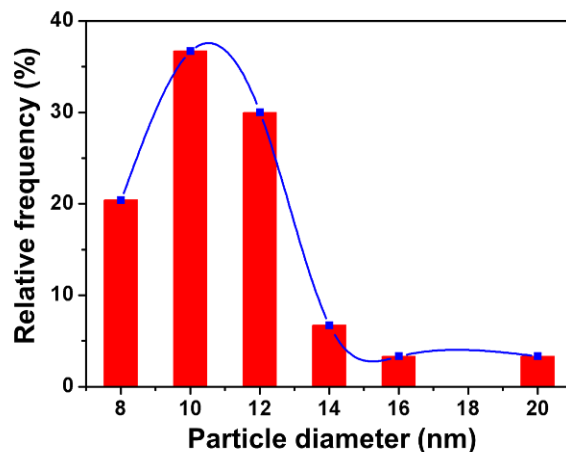


Figure S6. Statistical analysis of the diameters of the ultrafine V_2O_3 NPs in $V_2O_3/C-NTs/rGO$ indicating that their size ranged from 8 to 20 nm.

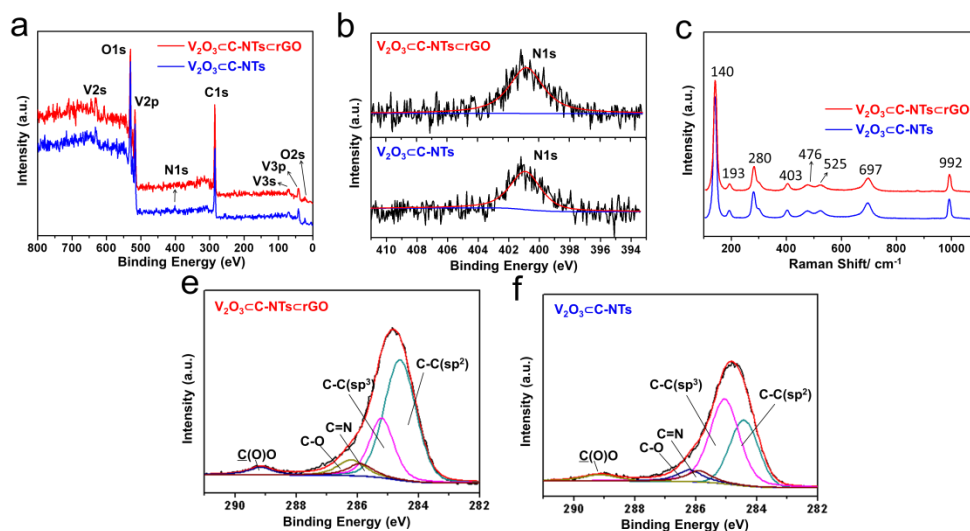


Figure S7. Composition and valence state characterization of $V_2O_3/C-NTs/rGO$ and $V_2O_3/C-NTs$. (a) XPS spectra of $V_2O_3/C-NTs$ and $V_2O_3/C-NTs/rGO$. (b) N1s XPS spectra of $V_2O_3/C-NTs$ and $V_2O_3/C-NTs/rGO$. (c) Raman spectra of $V_2O_3/C-NTs$ and $V_2O_3/C-NTs/rGO$. (e) C1s XPS spectra of $V_2O_3/C-NTs/rGO$ (e) and $V_2O_3/C-NTs$ (f).

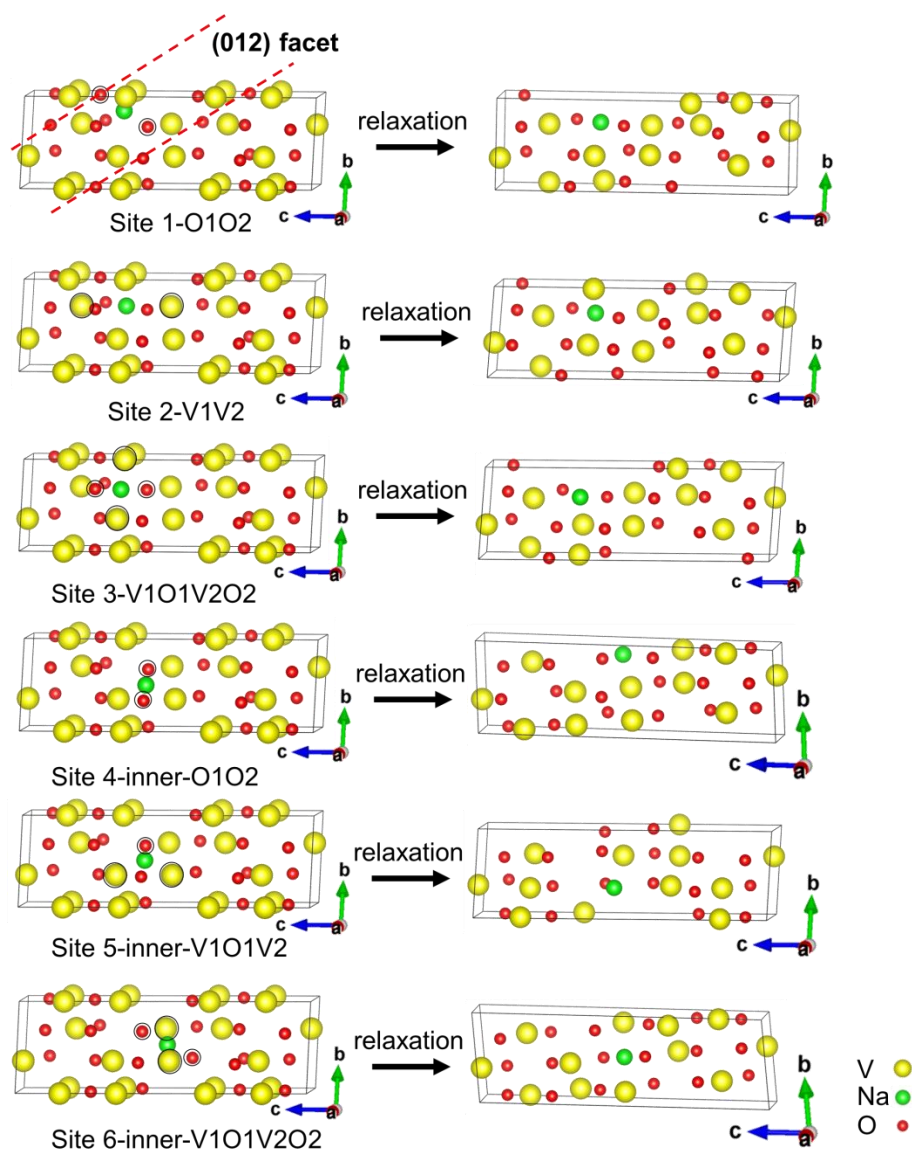


Figure S8. DFT calculation model of Na^+ ion insertion into V_2O_3 at different sites. Insertion into Site 1, Site 2 and Site 3 occurs in the interplanar space of the (012) facet. Site 1 is located between O1 and O2, Site2 is located between V1 and V2, and Site 3 is located in the quadrangle formed from two adjacent O atoms and two adjacent V atoms. Insertion into Site 4, Site 5 and Site 6 occurs in the inner of (012) facet. Site 4 is located between two O atoms in the inner of (012) layer, Site 5 is located in triangle formed from one O atom and two adjacent V atoms, and Site 6 is in the quadrangle formed from two adjacent O atoms and two adjacent V atoms.

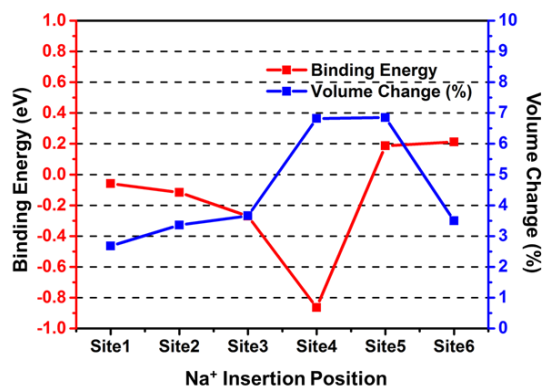


Figure S9. Statistics of the binding energy and volume change for Na⁺ ion insertion into the different sites.

Table S1. Cell volume changes and Na⁺ intercalation energies (E_i) based on the DFT calculations assuming Na⁺ intercalation into the V₂O₃ crystal.

Na ⁺ ion position	x	y	z	Total energy (eV)	Binding energy (eV)	Volume change (%)
V ₂ O ₃				-263.72355		
Site1-O1O2	0.67343	0.82656	0.66665	-263.78263	-0.05907	2.88
Site2-V1V2	0.33333	0.66667	0.66667	-263.8400	-0.11645	3.36
Site3-V1O1V2O2	0.83335	0.66666	0.66666	-263.99409	-0.27054	3.65
Site4-inner-O1O2	0.82657	0.49323	0.58333	-264.58743	-0.86388	6.82
Site5-inner-V1O1V2	0.66667	0.49321	0.58333	-263.53712	0.18643	6.85
Site6-inner-V1O1V2O2	0.5	0.5	0.5	263.51154	0.21201	3.46

DFT calculations. DFT calculations were performed to identify the most suitable host site for Na⁺ intercalation in the V₂O₃ crystal (space group: R-3c). During the discharge process, the most favorable geometry-optimized high-symmetry intercalation sites for 0.16 Na⁺ per unit formula in the V₂O₃ cell were considered theoretically (Figure S8). The Na⁺ intercalation energy (E_i) is defined as $E_i = E_{Na+V_2O_3} - E_{V_2O_3} - E_{Na}$, where $E_{Na+V_2O_3}$ and $E_{V_2O_3}$ are the total energies of the Na⁺-

intercalated and pristine V_2O_3 unit cell, respectively, while E_{Na} is the energy of isolated Na. The corresponding total energies, binding energies and volume changes are listed in Table S1. More negative values of the binding energy and small volume changes indicate that the Na atom prefers to insert into a specific site in V_2O_3 (Figure S9). If the Na^+ ion inserts into the inner of (012) plane of the (012) layer would expanded dramatically or be destroyed, owing to the large volume change. Despite this fact, the lowest binding energy was calculated for insertion of Na^+ into site 4. When the Na^+ ion inserts into the interplanar space of the (012) facet, the crystal structure is still ordered and symmetric. In addition, a low binding energy is calculated. These results demonstrated that the Na atom would occupy in the interplanar space of the (012) plane (sites 1-3) rather than the other sites in the inner of (012) facet (sites 4-6).

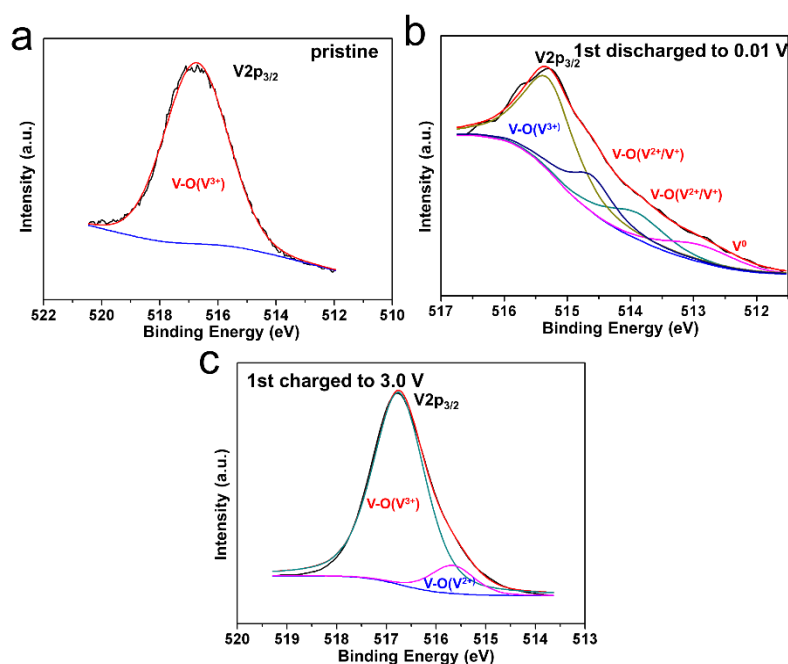


Figure S10. *Ex situ* V XPS spectra of $V_2O_3/C-NTs/rGO$ at different voltages. (a) Pristine $V_2O_3/C-NTs/rGO$, and $V_2O_3/C-NTs/rGO$ (b) the 1st discharge to 0 V and (c) the 1st charge to 3.0 V.

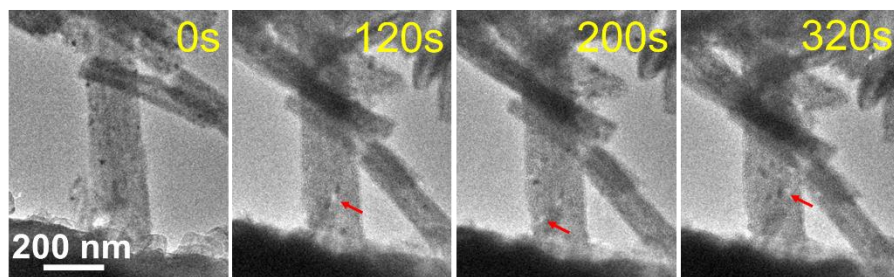


Figure S11. Structural evolution of the V_2O_3/C -NTs observed by *in situ* TEM.

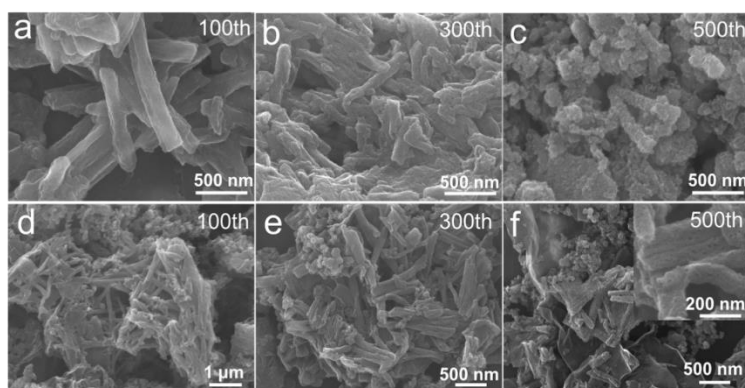


Figure S12. *Ex situ* SEM images of V_2O_3/C -NTs/rGO and V_2O_3/C -NTs. (a-c) SEM images of V_2O_3/C -NTs after the 100th (a), 300th (b) and 500th (c) cycle. In these *ex situ* SEM tests, acetylene black was not added into the electrode. (d-f) SEM images of V_2O_3/C -NTs/rGO after the 100th (d), 300th (e) and 500th (f) cycles. The inset of (f) is an SEM images of a porous carbon tube by etching the V_2O_3 NPs.

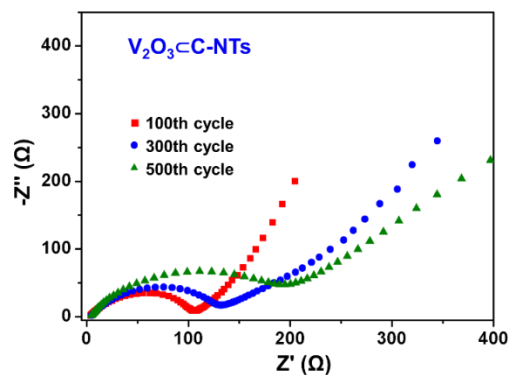


Figure S13. Nyquist plots of V_2O_3/C -NTs after the 100th, 300th, and 500th cycle.

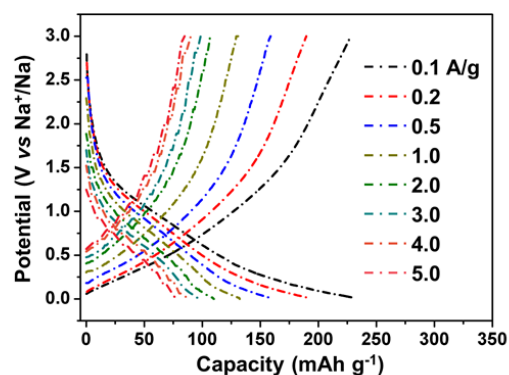


Figure S14. Rate capacities of rGO and N-doped C-NTs in SIB from 0.1 to 5 A g⁻¹. Based on CHN elemental analysis, the content of C-NTs and rGO in V₂O₃⊂C-NTs⊂rGO is 18%. Thus, the C-NTs and rGO contribute only low capacities of 41.4, 23.76 and 14.04 mAh g⁻¹ at 0.1, 1.0 and 5.0 A g⁻¹, respectively. The main capacity of V₂O₃⊂C-NTs⊂rGO is contributed by the sodiation of the V₂O₃ NPs.

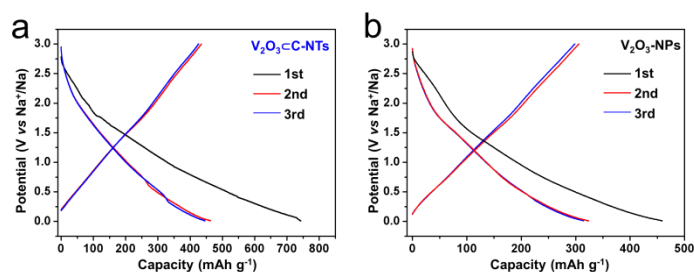


Figure S15. First three charge-discharge curves at 0.1 A g⁻¹. (a) V₂O₃⊂C-NTs, (b) V₂O₃-NPs.

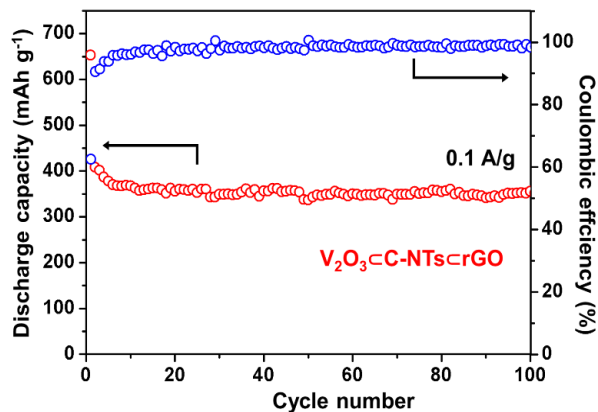


Figure S16. Cycling performance and corresponding coulombic efficiency of V_2O_3/C -NTs/rGO at 0.1 A g^{-1} from 0.01-3.0 V.

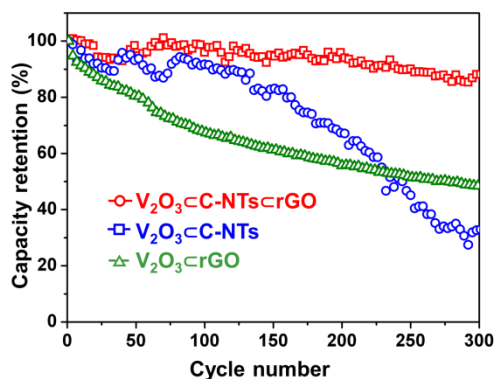


Figure S17. Capacity retention of V_2O_3/C -NTs/rGO, V_2O_3/C -NTs and V_2O_3/rGO at 1.0 A g^{-1} from 0.01-3.0 V. The electrochemical measurement parameters were the same as those for the other samples.

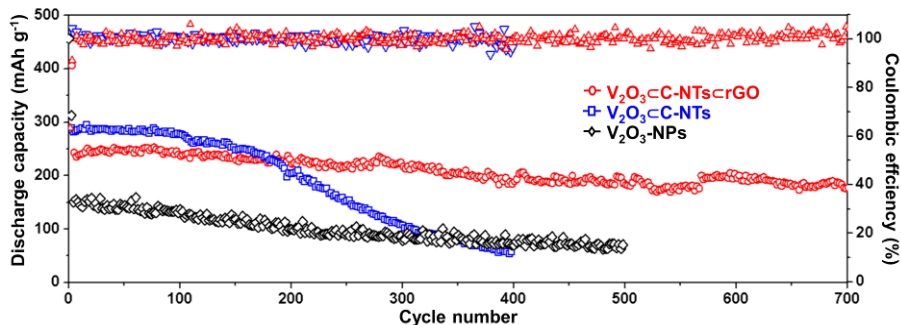


Figure S18. Cycling performance and corresponding coulombic efficiency of the three samples during 700 cycles at 5.0 A g^{-1} from 3.0–0.01 V.

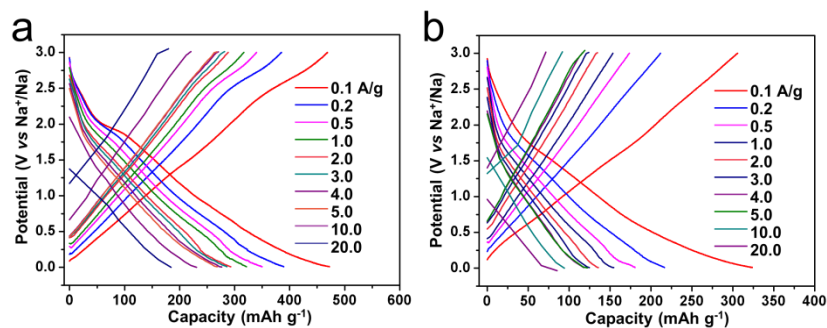


Figure S19. Charge-discharge curves of the three samples at different rates from 0.1 to 20 A g⁻¹.

(a) V₂O₃/C-NTs, (b) V₂O₃-NPs.

Table S2. Electrochemical performance of selected carbon-based conversion-type anodes.

Materials and Structure	Reversible capacity	Cycling stability	Rate capacity	Ref.
		(remaining capacity/cycles/current density)	(capacity/current density)	
Our work	413 mAh g ⁻¹ at 0.1 A g ⁻¹	250/ 1000 / 1 A g ⁻¹	210 / 10 A g ⁻¹	
		175 / 15000 / 5 A g ⁻¹	165 / 20 A g ⁻¹	
VO ₂ /rGO	202 mAh g ⁻¹ at 0.06 A g ⁻¹	~110 / 400 / 0.4 A g ⁻¹	100 / 0.8 A g ⁻¹	7
MoS ₂ /rGO	701 mAh g ⁻¹ at 0.02 A g ⁻¹	~227 / 300 / 0.32 A g ⁻¹	352 / 0.64 A g ⁻¹	10
Fe ₂ O ₃ /rGO	535 mAh g ⁻¹ at 0.1 A g ⁻¹	~150 / 200 / 1 A g ⁻¹	190 / 1 A g ⁻¹	5
MoS ₂ /rGO	338 mAh g ⁻¹ at 0.25 A g ⁻¹	~233/ 20 / 0.1 A g ⁻¹	~170 / 0.2 A g ⁻¹	8
Co ₃ S ₄ /rGO	423 mAh g ⁻¹ at 0.5 A g ⁻¹	329/ 50 / 0.5 A g ⁻¹	154 / 10 A g ⁻¹	11
WS ₂ @graphene	584 mAh g ⁻¹ at 0.02 A g ⁻¹	94/ 500 / 0.64 A g ⁻¹	~120 / 1.28 A g ⁻¹	12
3D MoS ₂ -rGO microspheres	574 mAh g ⁻¹ at 0.2 A g ⁻¹	323/ 600 / 1.5 A g ⁻¹	234 / 10 A g ⁻¹	13
Amorphous Fe ₂ O ₃ /graphene	350 mAh g ⁻¹ at 0.2 A g ⁻¹	110/ 500 / 2 A g ⁻¹	126 / 2 A g ⁻¹	14
NiS ₂ @graphene	611 mAh g ⁻¹ at 0.05 A g ⁻¹	~500/ 100 / 0.05 A g ⁻¹	216 / 2 A g ⁻¹	15
FeS ₂ microspheres on rGO	375 mAh g ⁻¹ at 0.09 A g ⁻¹	164/ 800 / 0.9 A g ⁻¹	195 / 4.5 A g ⁻¹	16
MoS ₂ embedded in CNTs	854 mAh g ⁻¹ at 0.1 A g ⁻¹	253/ 100 / 10 A g ⁻¹	224 / 20 A g ⁻¹	6
MnO NPs in carbon nanotubes	615 mAh g ⁻¹ at 0.2 A g ⁻¹	273/ 3000 / 5 A g ⁻¹	292 / 5 A g ⁻¹	17
CoS ₂ NPs in carbon nanofibers	537 mAh g ⁻¹ at 0.1 A g ⁻¹	~300/ 1000 / 1 A g ⁻¹	201 / 10 A g ⁻¹	18
NiS _x /CNT@C	450 mAh g ⁻¹ at 0.1 A g ⁻¹	~340/ 200 / 0.1 A g ⁻¹	143 / 5 A g ⁻¹	19
CoS@carbon	401 mAh g ⁻¹ at 0.1 A g ⁻¹	294/ 100 / 0.1 A g ⁻¹	235 / 5 A g ⁻¹	9
V ₂ O ₃ NPs@C	425 mAh g ⁻¹ at 0.1 A g ⁻¹	~133/ 1000 / 2 A g ⁻¹	149 / 2 A g ⁻¹	20
V ₂ O ₃ /KBs	350 mAh g ⁻¹ at 0.1 A g ⁻¹	~150/ 1000 / 1 A g ⁻¹	~150 / 1 A g ⁻¹	21
Dual carbon-confined Co ₉ S ₈	604 mAh g ⁻¹ at 0.3 A g ⁻¹	~556/ 500 / 0.3 A g ⁻¹	330 / 6.4 A g ⁻¹	22
NiSe ₂ -rGO-C nanofibers	516 mAh g ⁻¹ at 0.2 A g ⁻¹	468/ 100 / 0.2 A g ⁻¹	243 / 3 A g ⁻¹	23

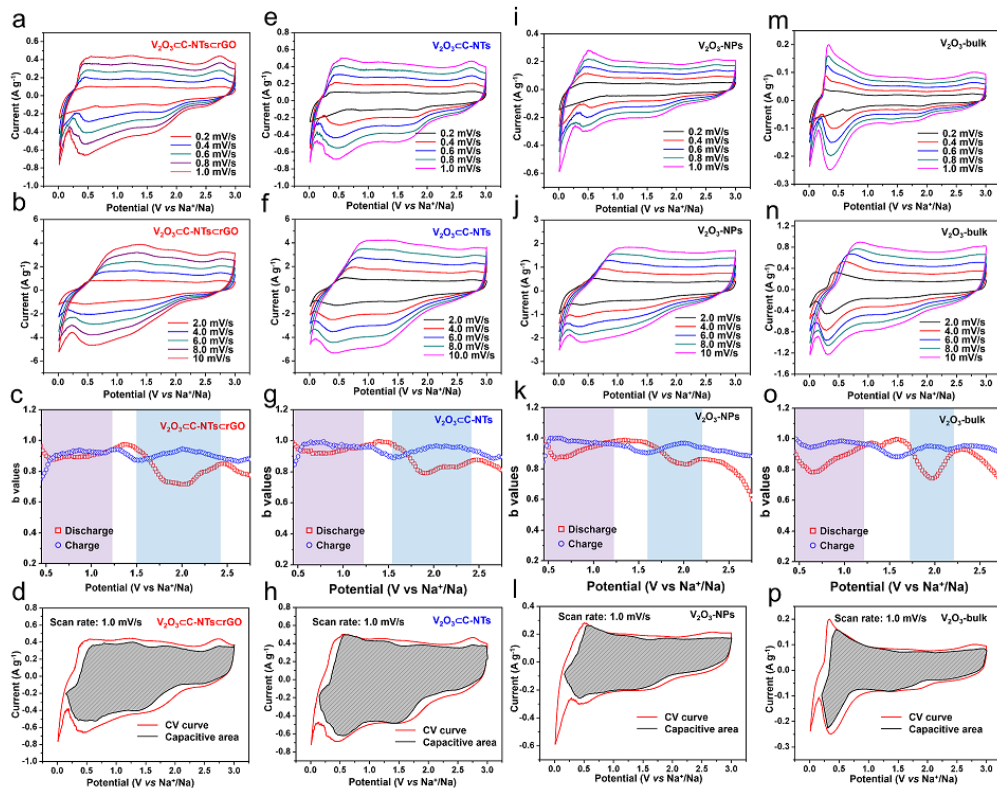


Figure S20. Kinetics and quantitative analysis. CV curves at various scan rates from 0.2 to 10 mV s^{-1} for $\text{V}_2\text{O}_3\text{-C-NTs-crGO}$ (a, b), $\text{V}_2\text{O}_3\text{-C-NTs}$ (e, f), $\text{V}_2\text{O}_3\text{-NPs}$ (i, j), and $\text{V}_2\text{O}_3\text{-bulk}$ (m, n). Plots of the b value vs potential for $\text{V}_2\text{O}_3\text{-C-NTs-crGO}$ (c), $\text{V}_2\text{O}_3\text{-C-NTs}$ (g), $\text{V}_2\text{O}_3\text{-NPs}$ (k), and $\text{V}_2\text{O}_3\text{-bulk}$ (o). CV curves of $\text{V}_2\text{O}_3\text{-C-NTs-crGO}$ (d), $\text{V}_2\text{O}_3\text{-C-NTs}$ (h), $\text{V}_2\text{O}_3\text{-NPs}$ (l), and $\text{V}_2\text{O}_3\text{-bulk}$ (p) at a scan rate of 1.0 mV s^{-1} . The shaded region shows the capacitive contribution.

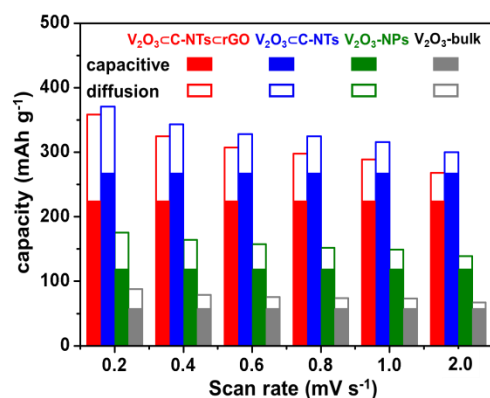


Figure S21. Statistics of the actual capacity contributions of the four samples showing the capacitive (shaded region) and diffusion-controlled (blank region) capacities of the four samples at different scan rates.

Kinetics and quantitative analysis. Figure S20 shows the CV curves of V₂O₃/C-NTs/rGO, V₂O₃/C-NTs, V₂O₃-NPs, and V₂O₃-bulk at various scan rates from 0.2 to 10 mV s⁻¹. Generally, the current response is a function of the sweep rate and can be expressed as Equation (1):

$$i(V) = av^b \quad (1)$$

where i is the current, V is the potential, v is the sweep rate (mV s⁻¹), and a and b are adjustable constants. When b is 1, the current is linearly related to v , arising from a capacitive-controlled process; if b is 0.5, the current results from a diffusion-controlled process and will follow semi-infinite linearity and therefore be proportional to $v^{1/2}$ (ref. 24). As shown in Figure S21c, the b values of V₂O₃/C-NTs/rGO present a broad peak above 1.5 V, where the lowest value is close to 0.6, which is similar to those of the V₂O₃/C-NTs, V₂O₃-NPs and V₂O₃-bulk (Figures S20g, k, o). With the reduction of the particle size, the potential range of the broad peak gradually increases, indicating that the NPs provide a larger Na⁺ ion diffusion interface than the bulk. Below 1.5 V, the b values of V₂O₃/C-NTs/rGO and V₂O₃/C-NTs stabilized at ~0.9, whereas that of V₂O₃-bulk gradually decreases to ~0.75. Moreover, the capacity contribution can be

further quantitatively separated into capacitive effects (k_1v) and diffusion-controlled reactions ($k_2v^{1/2}$), according to the Equation (2) (ref. 24):

$$i(V) = k_1 v + k_2 v^{1/2} \quad (2)$$

Figure S20d shows the CV profile for the estimated capacitive current of $V_2O_3/C-NTs/rGO$ (shaded region) at a scan rate of 1.0 mV s^{-1} , corresponding to a contribution of up to 77.7% of the total capacity. The capacitive capacity can arise from electrostatic or pseudocapacitive behaviors, which needs to be further distinguished. Generally, an electric double-layer capacitance value of $\sim 10 \text{ } \mu\text{F cm}^{-2}$ is assumed [25, 26]. Therefore, based on the SSA of $151.5 \text{ m}^2 \text{ g}^{-1}$ of the $V_2O_3/C-NTs/rGO$, an electric double-layer capacitance of $\sim 15.15 \text{ F g}^{-1}$ ($\sim 12.59 \text{ mAh g}^{-1}$ in 0.01-3.0 V) could be calculated. This value is 3.1% of the total obtained capacity at 0.1 A g^{-1} , indicating the capacitive capacity is largely dependent on the pseudocapacitive faradaic conversion process. Figure S21 shows the actual capacitive (shaded region) and diffusion-controlled (blank region) capacities for the four samples at different scan rates. Both the capacitive-controlled and diffusion-controlled capacities of the $V_2O_3/C-NTs/rGO$ and $V_2O_3/C-NTs$ are much larger than those of the V_2O_3-NPs and V_2O_3 -bulk.

Reference

- [1] G. Kresse, D. Joubert, *Phy. Rev. B* **1999**, 59, 1758.
- [2] G. Kresse, J. Furthmüller, *Phys. Rev. B* **1996**, 54, 11169.
- [3] G. Kresse, J. Furthmüller, *Comp. Mater. Sci.* **1996**, 6, 15-50.
- [4] J. Perdew, K. Burke, M. Ernzerhof, *Phys. Rev. Lett.* **1996**, 77, 3865.
- [5] Z. L. Jian, B. Zhao, P. Liu, F. J. Li, M. B. Zheng, M. W. Chen, Y. Shi, H. S. Zhou, *Chem. Commun.* 2014, 50, 1215.
- [6] C. B. Zhu, X. K. Mu, P. A. van Aken, Y. Yu, J. Maier, *Angew. Chem. Int. Ed.* **2014**, 53, 2152.
- [7] G. He, L. Li, A. Manthiram, *J. Mater. Chem. A* **2015**, 3, 14750.

- [8] L. David, R. Bhandavat, G. Singh, *ACS Nano* **2014**, *8*, 1759.
- [9] C. Wu, Y. Jiang, P. Kopold, P. A. van Aken, J. Maier, Y. Yu, *Adv. Mater.* **2016**, *28*, 7276.
- [10] X. Q. Xie, Z. M. Ao, D. W. Su, J. Q. Zhang, G. X. Wang, *Adv. Funct. Mater.* **2015**, *25*, 1393.
- [11] Y. Du, X. Zhu, X. Zhou, L. Hu, Z. Dai, J. Bao, *J. Mater. Chem. A*, **2015**, *3*, 6787.
- [12] D. W. Su, S. X. Dou, G. X. Wang, *Chem. Commun.* **2014**, *50*, 4192.
- [13] S. H. Choi, Y. N. Ko, J. K. Lee, Y. C. Kang, *Adv. Funct. Mater.* **2015**, *25*, 1780.
- [14] D. Li, J. S. Zhou, X. H. Chen, H. H. Song, *ACS Appl. Mater. Interfaces* **2016**, *8*, 30899.
- [15] T. Li, A. Q. Qin, L. L. Yang, J. Chen, Q. F. Wang, D. H. Zhang, H. X. Yang, *ACS Appl. Mater. Interfaces* **2017**, *9*, 19900.
- [16] W. H. Chen, S. H. Qi, L. Q. Guan, C. T. Liu, S. Z. Cui, C. Y. Shen, L. W. Mi, *J. Mater. Chem. A* **2017**, *5*, 5332.
- [17] Y. Z. He, P. Xu, B. Zhang, Y. C. Du, B. Song, X. J. Han, H. S. Peng, *ACS Appl. Mater. Interfaces*, **2017**, DOI: 10.1021/acsami.7b09559.
- [18] Y. L. Pan, X. D. Cheng, Y. J. Huang, L. L. Gong, H. P. Zhang, *ACS Appl. Mater. Interfaces* **2017**, *9*, 35820.
- [19] F. P. Zhao, Q. F. Gong, B. Traynor, D. Zhang, J. J. Li, H. L. Ye, F. J. Chen, N. Han, Y. Y. Wang, X. H. Sun, Y. G. Li, *Nano Res.* **2016**, *9*, 3162.
- [20] Y. S. Cai, G. Z. Fang, J. Zhou, S. N. Liu, Z. G. Luo, A. Q. Pan, G. Z. Cao, S. Q. Liang, *Nano Res.* **2017**, DOI 10.1007/s12274-017-1653-9.
- [21] X. X. An, H. L. Yang, Y. P. Wang, Y. Tang, S. Q. Liang, A. Q. Pan, G. Z. Cao, *Sci. China Mater.* **2017**, *60*, 717.
- [22] Z. L. Chen, R. B. Wu, M. Liu, H. Wang, H. B. Xu, Y. H. Guo, Y. Song, F. Fang, X. B. Yu, D. L. Sun, *Adv. Funct. Mater.* **2017**, *27*, 1702046.
- [23] J. S. Cho, S. Y. Lee, Y. C. Kang, *Sci. Rep.* **2016**, *6*, 23338.

- [24] T. C. Liu, W. G. Pell, B. E. Conway, S. L. Roberson, *J. Electrochem. Soc.* **1998**, 145, 1882.
- [25] B. Lesel, J. Ko, B. Dunn, S. Tolbert, *ACS Nano* **2016**, 10, 7572.
- [26] D. Sheberla, J. C. Bachman, J. S. Elias, C. J. Sun, S. H. Yang, D. Mircea, *Nat. Mater.* 2016, 16, 220.